Journal of Marine Science and Technology, Vol. 24, No. 6, pp. 1171-1180 (2016)
DOI: 10.6119/JMST-016-1026-6

INTERPRETATION OF SAR IMAGE MODULATION BY THE INTERACTION OF CURRENT AND BOTTOM TOPOGRAPHY IN GYEONGGI BAY WITH MICROWAVE SCATTERING MODELS

Tae-Ho Kim[1,2], Chan-Su Yang[1,2,3], and Kazuo Ouchi[4]

Key words: bottom topography, ocean surface current, microwave scattering model, method of moments, SAR.

ABSTRACT

The effect of the interaction between surface currents and bottom topography to the radar cross section (RCS) is investigated using theoretical and numerical scattering models and synthetic aperture radar (SAR) data. First, the ocean waveheight spectrum perturbed by a varying surface current is computed under the wind condition at the time of SAR data acquisition. The surface current data are extracted from the tidal current models. The RCS modulations are then computed using the small perturbation method (SPM) and the numerical scattering model based on the method of moments (MoM) with undulated surface height profiles simulated from the perturbed wave spectrum using the Monte-Carlo method. The RCS modulation relative to the RCS from the surrounding ambient sea surface is used to evaluate the two scattering models, and comparison of the results with X- and C-band data shows that the SPM underestimates the SAR data and that the MoM yields better agreement with the error of 11% in the relative RCS peak value and the peak displacement of 750 m with respect to the observed position. Although there still exist some discrepancy in the RCS modulation, the present results show the potential of the numerical approach based on the MoM and Monte-Carlo simulation for analysing the interaction between ocean current and bottom topography.

Paper submitted 05/27/16; revised 06/16/16; accepted 10/31/16. Author for correspondence: Chan-Su Yang (e-mail: yangcs@kiost.ac.kr).
[1] Department of Integrated Ocean Sciences, Korea University of Science and Technology, Republic of Korea.
[2] Marine Safety Research Center, Korea Institute of Ocean Science and Technology, Republic of Korea.
[3] Department of Convergence Study on the Ocean Science and Technology, Ocean Science and Technology School, Republic of Korea.
[4] Space Development Department, IHI Corporation, Japan.

I. INTRODUCTION

Synthetic Aperture Radar (SAR) is a powerful sensor for ocean remote sensing, and a substantial number of studies have been reported on the measurements of oceanic phenomena (e.g., Kerbaol and Collard, 2005; Ouchi, 2013), including underwater objects such as bottom topography (BT) (Alpers and Hennings, 1984; Hennings, 1998; Calkoen et al., 2001; Kim, 2006; Kim et al., 2009; Fan et al., 2011), internal waves (Alpers, 1985; Jackson and Apel, 2004; Jackson et al., 2013; Hong et al., 2015), and man-made marine cultivation fields (Sugimoto et al., 2013; Won et al., 2013).

The imaging mechanism of sea BT by radar was first proposed by Alpers and Hennings (1984). In shallow waters, the surface current varies depending on water depth, and to the first order, the current velocity is governed by the continuity equation. The varying surface current then perturbs the small-scale ocean waves, and SAR detects the microwave backscattered from the perturbed ocean waves of varying surface roughness. Thus, the SAR images of BT are indirectly related to BT through these processes, and therefore, the models of microwave backscatter, current-wave interaction, and current velocity and BT are required to interpret the SAR image modulation by BT.

Over the last few decades, theoretical and numerical microwave scattering models have been developed to describe the radar backscatter from rough surface (Valenzuela, 1978; Romeiser et al., 1997a; Tsang et al., 2001). Among these models, several models were used to reproduce the variation of the radar cross section (RCS) from the sea surface of varying surface currents (Shuchman et al., 1985; Holliday et al., 1986; Romeiser et al., 1997b; Vogelzang, 2001; Li et al., 2009, Kim et al., 2014). In some papers, the comparison results with the multi frequency SAR data show good agreement at L-band, but tend to underestimate the observed RCS at C- and X-band (Holliday et al., 1986; Romeiser et al., 1997b; Vogelzang, 2001). Thus, further studies are required for the understanding of C- and X-band radar backscatter from the sea surface over varying BT.

In this paper, preliminary results are presented using the method of moment (MoM) and small perturbation method (SPM)

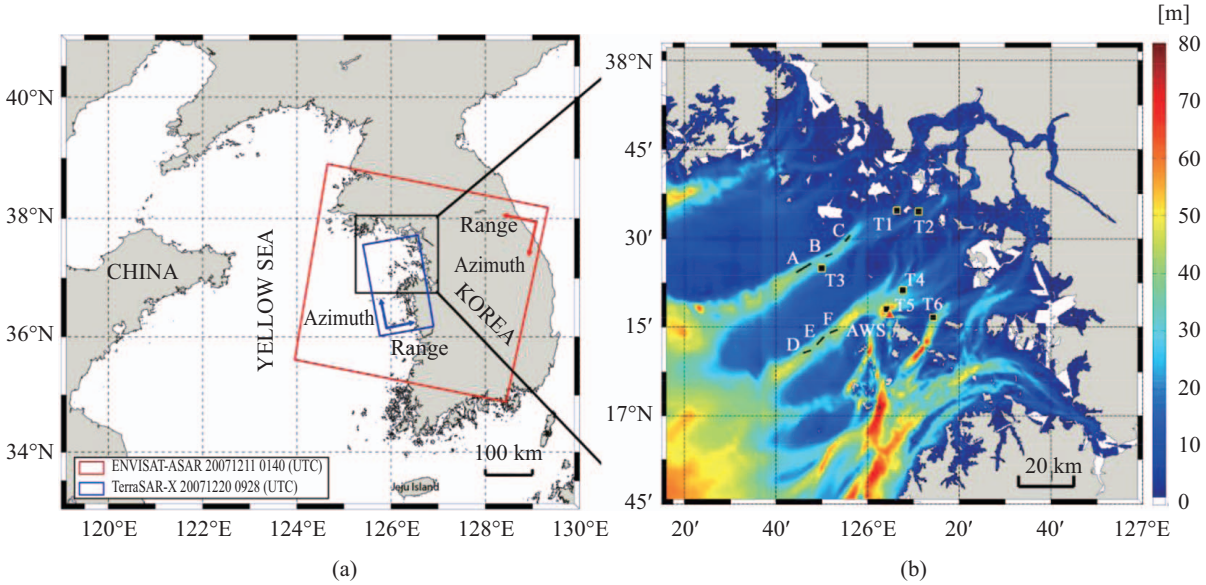

Fig. 1. Coverage map of satellite images and study area. (a) The red and blue boxes represent the coverage of ENVISAT-ASAR and TerraSAR-X respectively. (b) The color map represents water depth from 0 to 40 m. The A-F lines indicate slope of BT at each site and the red triangular mark just below right of T5 is the location of AWS. The rectangular marks represent observation site of tidal current.

for modelling radar backscatter and the Monte-Carlo method to simulate the ocean surface perturbed by the varying surface current. Note that the SPM has generally been used by many researchers, but the MoM has not been used previously for analysing the SAR images of BT, and the present study is the first attempt based on this approach. The wind and tidal current data used in the scattering models were extracted from the Automatic Weather System (AWS) and tidal current models respectively. The RCS modulations computed by both the MoM and SPM were then compared with the C- and X-band SAR data over the shallow waters in the west coast of Korean peninsula.

The paper is organized as follows. In section 2, the characteristics of the study area and SAR imaging mechanism by BT are described, and in section 3, the SAR data used in this study are presented, followed by the brief description of the MoM and SPM in section 4. In section 5, the comparison results between computed and SAR data are described, and conclusions are given in section 6.

II. STUDY AREA AND IMAGING PROCESS

The area under study is the Gyeonggi-bay on the mid-west coast of Korea as shown in Fig. 1(a), where the surface current is dominated by strong tidal current in a northeast-southwest direction produced by high tidal changes. The water depth in this area is 20 m on average and becomes deeper gently toward the southwest direction (Fig. 1(b)). This area has complex geological characteristics with many islands and a tidal channel over a depth of 30 m (Lee et al., 2009). These conditions generate the strong interaction between the surface current velocity and BT, and the convergence or divergence front frequently appear in the SAR images (Kim, 2006; Kim et al., 2009).

The interaction of surface current with BT is very complex. The previous researches proposed several mechanisms for the convergence or divergence of surface water, such as, the tidal current interaction with BT, the effect of horizontal and vertical density gradients (Hennings, 1998; Valle-Levinson et al., 2000). Alpers and Hennings (1984) described a simplified imaging process using the 1-D continuity equation. They assumed that the variation of surface current speed above the BT is only affected by the horizontal current gradient, and the orthogonal current component normal to the direction of the ridge axis obeys the continuity equation. Kim et al. (2009) showed that the convergence of surface current flow in the Gyeonggi-bay is weakly dependent on the density variation. Hence, we assumed that the SAR imaging mechanism for surface roughness modulation in the Gyeonggi-bay is dominated by the 1-D continuity equation. However, we have to note that this algorithm includes the assumption of a constant parallel velocity component, which may induce some error. As illustrated in Fig. 2, when a steady current comes to a hill of sea bottom, the current speed increases, and the surface becomes smooth yielding little radar backscatter. At an edge of the sea valley, water mass drops toward the seabed, and the surface current slows down, creating a current converging zone where the surface becomes rough. The radar backscatter and hence the SAR image modulation is large in this converging zone.

III. DATA DESCRIPTION

1. Water Depth

The depth profiles over BT were extracted by General Bathymetric Chart of the Ocean (GEBCO, http://www.gebco.net/)

Table 1. Parameters of SAR and wind data at the AWS station closest to the bright fronts.

Satellite/Frequency	ENVISAT-ASAR/5.3 GHz (C-band)	TerraSAR-X/9.65 GHz (X-band)
Acquisition time (UTC)	2007.12.11 01:40	2007.12.20 09:28
Mode/Polarization	Wide Swath/VV	ScanSAR/VV
Center incidence angle [deg]	30.89	36.56
Nominal resolution [m] (range/azimuth)	150/150	18.5/18.5
Wind speed [m/s]	2.68	2.61
Wind direction [deg]	321.7	52.3

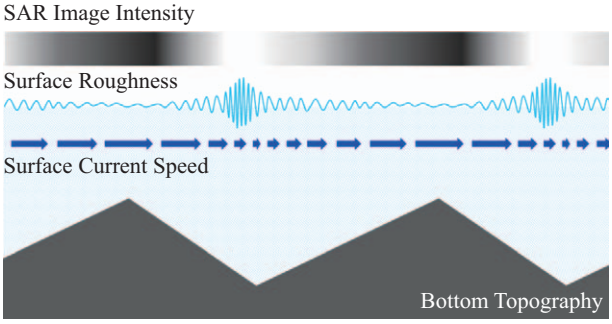

Fig. 2. Schematic of the imaging mechanism of BT (Alpers and Hennings, 1984).

and interpolated bathymetric grid data (Seo, 2008) (Fig. 1(b)). The spatial resolutions of GEBCO and re-analysis model are 0.0084 and 0.0028 deg, respectively. To increase the spatial resolution, we interpolated the water depth using both models data. From interpolated water depth, we can see clearly the two main channels of bottom topography in Fig. 1(b). In describing the interaction between BT and current, we consider only the orthogonal component, i.e., cross direction of the underwater ridge or crest axis, of the current obeys the continuity equation as by Alpers and Hennings (1984). For defining the orthogonal current component, we selected six front lines of same topography gradient as indicated by black lines A-F in Fig. 1(b).

2. Satellite and Wind Data

Figs. 3(a) and 3(b) show ENVISATR-ASAR (December 11, 2007. 01:40 (UTC)) and TerraSAR-X (December 20, 2007. 09:28 (UTC)) VV-polarization amplitude images of region of interest respectively. These SAR data were used to compare the simulation results. The geometric correction was performed using the Next ESA SAR Toolbox (https://earth.esa.int/web/nest/home/). Table 1 shows the radar frequency, data acquisition time, sensor mode, polarization, incidence angle and spatial resolution. The wind direction and speed averaged over 10 minutes at the AWS station closest to the bright fronts were used for RCS simulation.

The averaged wind data acquired by the AWS (Fig. 1(b)) were provided by the Korea Meteorological Administration (KMA). The observed wind speed and direction were 2.68 m/s and 321.7° at the time of ENVISAT-ASAR data acquisition, and 2.61 m/s and 52.3° at the time of TerraSAR-X data acquisition (Table 1).

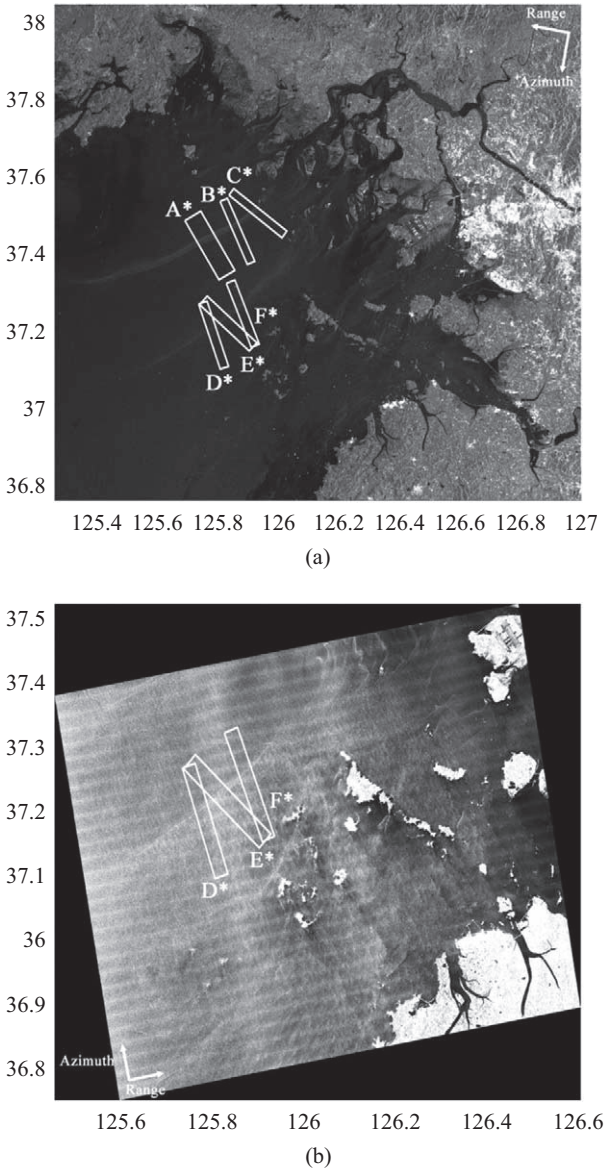

Fig. 3. SAR amplitude images. (a) ENVISAT-ASAR (VV-pol.) at 01:30 (UTC) on December 11, 2007. (b) TerraSAR-X (VV-pol.) at 09:28 (UTC) on December 20, 2007. White boxes represent the areas used to extract the SAR intensity, water depth and current speed.

3. Current Data

In order to get the surface tidal current data at the time of each

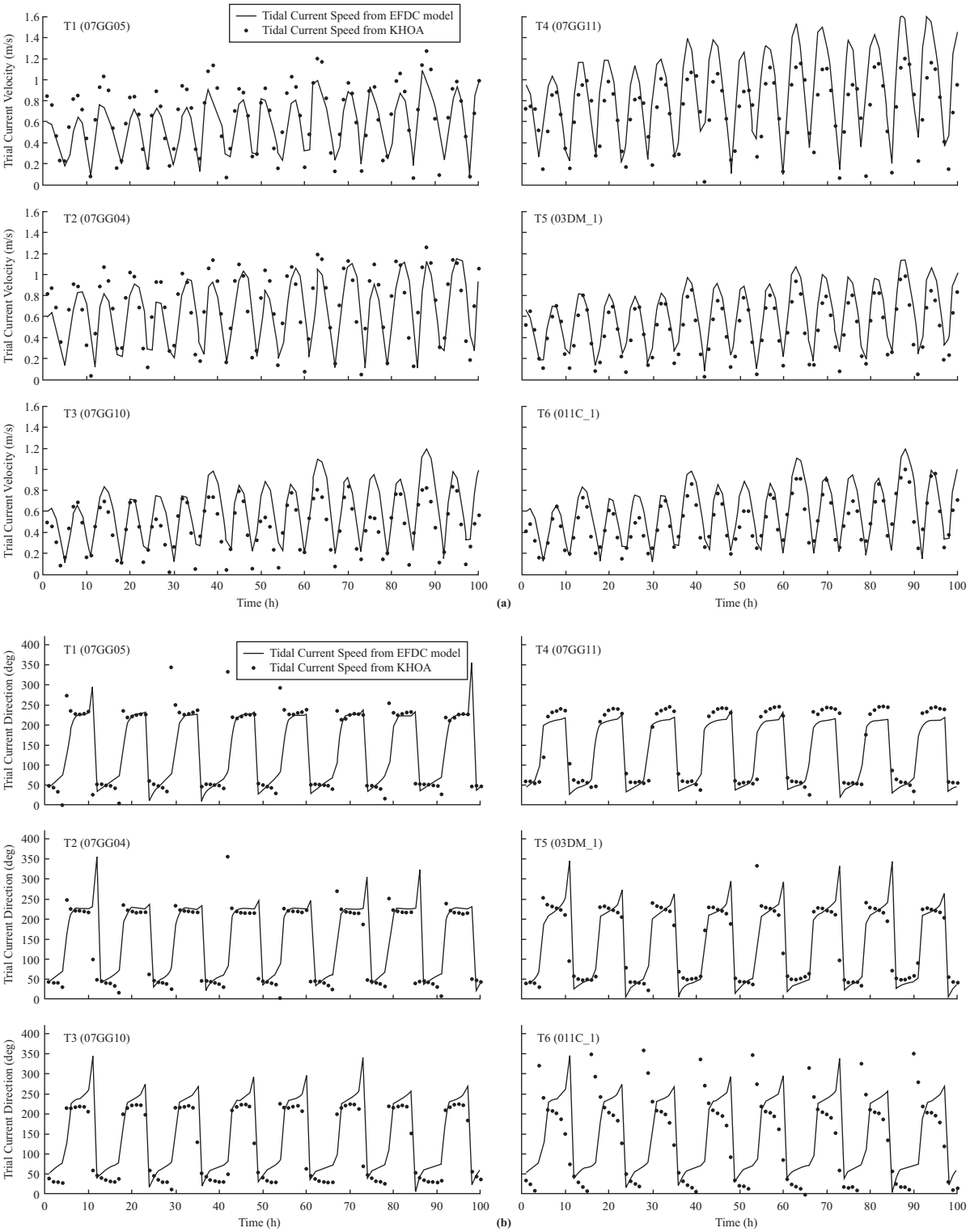

Fig. 4. Comparison of (a) speed and (b) direction from EFDC model and KHOA tidal current data. The solid lines and dots represent the EFDC model and KHOA data, respectively.

SAR data, we used two types of tidal model. The Environmental Fluid Dynamics Code (EFDC) model was used to generate the surface current in Gyeonggi-bay at the time of ENVISAT-ASRA image acquisition on December 11 2007 (Kim et al., 2014). The model was implemented with the Yamada level 2.5 turbulence closure scheme, and applied to the tidal flow, salinity, temperature and wind-driven flow (Yang et al., 2009). The tidal current data at TerraSAR-X data is acquisition time extracted

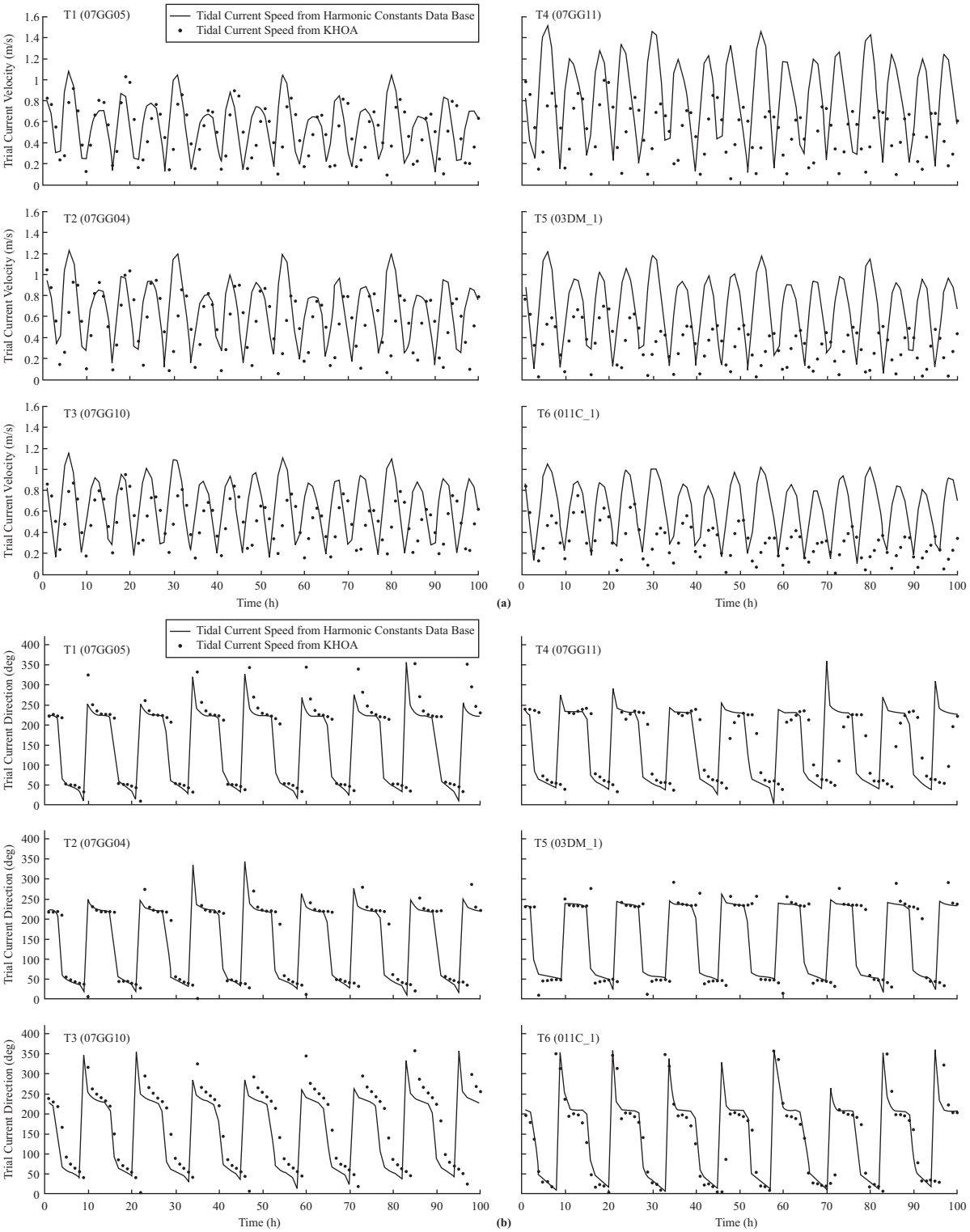

Fig. 5. Comparison of (a) speed and (b) direction from harmonic constants data base and KHOA tidal current data. The solid lines and dots represent the harmonic constants data base and KHOA data, respectively.

by harmonic constants dataset derived from the unstructured-mesh-based (FDM) and square-mesh-based (FEM) tidal models (Min et al., 2011). Note that the latter is a barotropic tidal current. The tidal current velocity and direction extracted from EFDC and harmonic constants data base were compared with time series from the current data, which were provided by the Korea Hydrographic and Oceanographic Administration (KHOA). The observation site of KHOA tidal data is shown in Fig. 1(b)

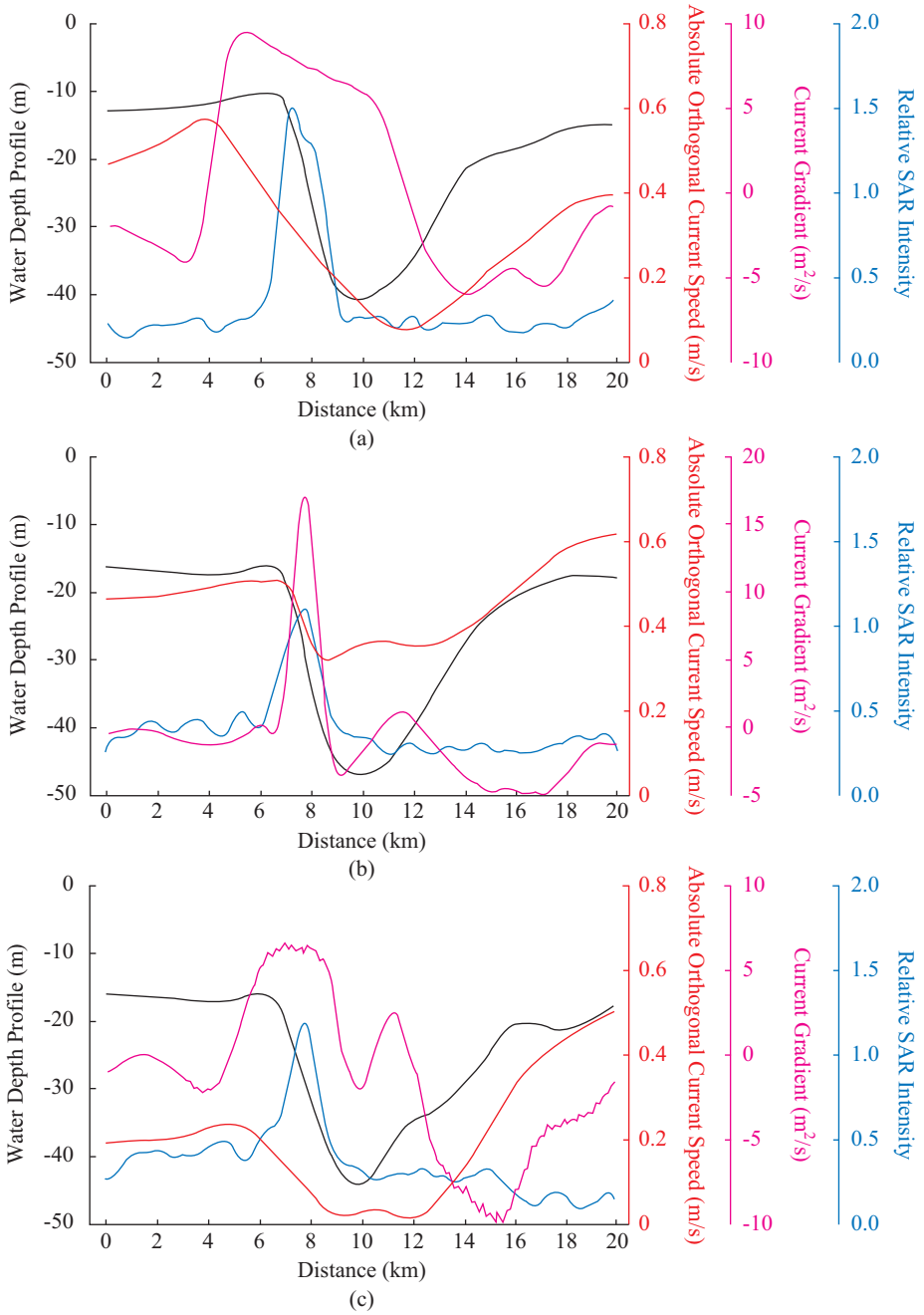

Fig. 6. Comparison of water depth (black), orthogonal current speed (red), orthogonal current gradient (magenta) and relative SAR intensity (blue). The graphs (a) and (b) show the results at strips A* and D* in the ENVISAT-ASAR data respectively, and (c) at E* in the TerraSAR-X data.

as black rectangular marks, and the Figs. 4 and 5 represent the comparison results between tidal models and KHOA data. Although there are some discrepancies, fairly good agreements can be seen in both at the tidal current speed and direction at all observation positions.

4. Comparison of Depth, SAR and Current

The data of selected areas enclosed by white strips A*, D* and E* in representing ENVISAT-ASAR data and at strip E* in the TerraSAR-X data, respectively in Fig. 3 are used here to depict the analysis. The strips had a same width and slope gradient (Fig. 1(b), A-F) with 20 km length in the direction perpendicular to each gradient line.

Fig. 6 shows the results of water depth, orthogonal current speed, orthogonal current gradient and relative SAR intensity at the selected locations as represented by strips A*, D* and E*. The relative RCS means the ratio of RCS perturbed by varying current to that of ambient sea surface. Note that all profiles in Fig. 6 are averaged and smoothed from all lines in each strip. According to the continuity equation, the position of minimum

current speed should correspond to the position of maximum water depth, and therefore, the water depth modulation peak should be, in principle, at the same position as that of minimum current (Alpers and Hennings, 1984). However, in this study the modulation peaks are found to be shifted to some extents from the location of the maximum water depth for all cases. This phenomenon moderately matches for Figs. 6(b) and 6(c) where the locations of orthogonal current speed were measured their minimum at 8.5 km and 10.5 km, respectively, which are very close to the distance for peaks in water depth at 7 km for both locations. However, in case of Fig. 6(a) the difference in distance between the locations of minimum orthogonal current speed and maximum depth is much (around 5.5 km). These offsets may be caused by the rapid variation of water depth. Nevertheless, the results show overall reasonable agreement between the locations of highest relative intensity and the minimum value of orthogonal current. Similarly, the case of Fig. 6(a) shows larger positional difference (4.5) between the locations of maximum SAR data (7.2 km) and minimum current (11.7 km) than the other two cases, and this might have resulted in the positional discrepancy of model result. In contrast to the orthogonal current speed, the orthogonal current gradient (m^2/s) can be described well in comparison to relative SAR intensity as they have shown matches at their peaks for corresponding locations in cases of Fig. 6(b) and 6(c) except for that of Fig. 6(a). The extracted current speeds were used as input data to the radar backscattering model.

IV. NUMERICAL RADAR BACKSCATTERING MODEL

1. Random Roughness Surface

Random rough surfaces are generated in accordance with a perturbed waveheight spectrum. A simulated surface has a length L, divided into independent segments of N points separated by a distance Δx. The surface height profile at each segment can be generated as follows (Tsang et al., 2001):

$$f(x_n) = \frac{1}{L}\sum_{m=-N/2}^{N/2-1} F(\mathbf{K}, \mathbf{r}) e^{ix_n k_m}$$
$$x_n = n\Delta x (n = 1, 2, 3, \ldots, N) \tag{1}$$

where

$$F(\mathbf{K}, \mathbf{r}) = [2\pi L \Psi(\mathbf{K}, \mathbf{r})]^{0.5} r_m \tag{2}$$

In the above equations, x_n is the location of each segment in the orthogonal direction to the ridge axis. In the scattering models, the random surface is generally described by Gaussian, exponential and fractal geometry functions (Tsang et al., 2001; Franceschetti et al., 2000). In this paper, we assumed a Gaussian random rough surface using a random variable r_m, having a zero-mean and unit-variance Gaussian distribution. As mentioned before, we assumed that the variation of surface roughness obeys the current velocity changing over normal to the direction of the ridge axis. This interaction can be described by a perturbed waveheight spectrum, $\Psi(\mathbf{K}, \mathbf{r})$, at a position $\mathbf{r} = (x, y)$. Eq. (1) was computed using a fast Fourier transform (FFT) technique.

2.Ocean Waveheight Spectrum

The Pierson-Moskowitz spectrum used in this study applies to the fully developed sea, and can be expressed as (Broschat, 1999),

$$\psi_0(k_m) = \frac{\alpha}{4|k_m|^3} \exp\left\{-\frac{\beta g^2}{k_m{}^2 U_{19.5}{}^4}\right\} \tag{3}$$

where $k_m = 2\pi m/L$ is the wavenumber, $U_{19.5}$ is the wind speed at a height of 19.5 m, g is the gravitational acceleration, and other constants α, β are 0.0081 and 0.74 respectively. The waveheight spectrum perturbed by the interaction of currents with BT can be obtained from Eq. (3) and the action balance equation as follows (Hughes, 1978; Ouchi, 1994)

$$\psi(\mathbf{k}, \mathbf{r}) = \psi_0(\mathbf{k})\left[1 + \frac{\hat{\mathbf{k}}}{k_m}\left\{\frac{2\beta g^2}{k_m{}^3 U_{19.5}{}^4} + \frac{c_g(k_m)}{c_p(k_m)} - 4\right\}\frac{1}{\mu(\mathbf{k})}\hat{\mathbf{k}}\cdot\frac{\partial U(\mathbf{r}, t)}{\partial \mathbf{r}}\right] \tag{4}$$

where $\psi_0(\mathbf{k}) = \hat{\mathbf{k}}\psi_0(k_m)$, $\hat{\mathbf{k}}$ is the unit vector of surface wave. $c_g(k_m) = \partial\omega_0(k_m)/\partial k_m$ is the wave group velocity, $c_p(k_m) = \omega_0(k_m)/k_m$ is the wave phase velocity, and $\mu(\mathbf{k}) = 0.04 k_m{}^2 u_* \Theta(\theta)/\omega(k_m)$ is the spectral relaxation rate. $\mathbf{U}$ and u_* are the current vector and the friction velocity respectively.

3. Computation of Radar Cross Section

1) Numerical Simulation Based on MoM

Based on the electromagnetic scattering theory, the scattered electric and magnetic fields can be calculated by the combined field integral equation (CFIE). The CFIE can be derived as the function of the equivalent electric and magnetic surface current (J_0, M_0), which are induced by incidence electric and magnetic fields, with a boundary condition between air and water layers, C_0. It can be solved by Eqs. (5a) and (5b) for a horizontally polarized incident field (Franceschetti et al., 2000).

$$-ik_0 Z_0 \int_{c_0} J_0(\bar{\rho}')G_0(\bar{\rho}, \bar{\rho}')dl' + \int_{c_0} M_0(\bar{\rho}')\hat{n}_0\cdot\nabla' G_0(\bar{\rho}, \bar{\rho}')dl' - \frac{1}{2}M_0(\bar{\rho}) = -E^i(\bar{\rho}) \tag{5a}$$

$$-ik_1 Z_1 \int_{c_0} J_0(\bar{\rho}')G_1(\bar{\rho}, \bar{\rho}')dl' + \int_{c_0} M_0(\bar{\rho}')\hat{n}_0\cdot\nabla' G_1(\bar{\rho}, \bar{\rho}')dl'$$

$$-ik_1 Z_1 \int_{c_0} J_1(\bar{\rho}')G_1(\bar{\rho}, \bar{\rho}')dl' + \int_{c_0} M_1(\bar{\rho}')\hat{n}_1 \cdot \nabla' G_1(\bar{\rho}, \bar{\rho}')dl' - \frac{1}{2}M_0(\bar{\rho}) = 0 \quad (5b)$$

where $Z_{0,1}$ are the air- and sea-space wave impedances. $G_n(\bar{\rho}, \bar{\rho}') = \frac{i}{4}H_0^{(i)}\left(k_n|\bar{\rho} - \bar{\rho}'|\right)$, $H_0^{(i)}$ is the zeroth-order Hankel function of the first-kind; $\bar{\rho}$ and $\bar{\rho}'$ are the position vectors for observation and source points, respectively. l is the surface profile. Note that the apostrophe mark ($'$) represents operation for source point terms only. Eqs. (5a) and (5b) defined the relationship between the incident and scattered wave for outside and inside of the scatterer. Eq. (5a) describes the evaluation of the electric field in the air layer. Eq. (5b) represents the integral equation that computes the electric field in the ocean layer with the boundary conditions at C_0. The equivalent electric and magnetic surface currents on the boundaries can be determined by using the following numerical simulation procedure.

Eqs. (5a) and (5b) can be expressed as the following matrix equation using pulse basis function, and the point matching technique with n^{th} observation and m^{th} source points (Franceschetti et al., 2000):

$$\begin{bmatrix} [\boldsymbol{Z}_{11}{}^{nm}] & [\boldsymbol{Z}_{12}{}^{nm}] \\ [\boldsymbol{Z}_{21}{}^{nm}] & [\boldsymbol{Z}_{22}{}^{nm}] \end{bmatrix} \begin{bmatrix} [\boldsymbol{I}_1{}^{n}] \\ [\boldsymbol{I}_2{}^{n}] \end{bmatrix} = \begin{bmatrix} [\boldsymbol{V}_1{}^{m}] \\ [0] \end{bmatrix} \quad (6)$$

Each elements of the impedance matrix [$\boldsymbol{Z}$] can be computed by using Eqs. (2.3)-(2.7) in Franceschetti et al. (2000). The unknown surface current component [$\boldsymbol{I}$] can be calculated by the matrix equation with the excitation vector [$\boldsymbol{V}$]. After the computation with the unknown variable at the current component in Eq. (6), the scattered field can be computed by using the equivalent electric and magnetic surface currents as follows

$$E^s = -ik_0 Z_0 \int_{c_0} J_0(\bar{\rho}')G_0(\bar{\rho}, \bar{\rho}')dl' + \int_{c_0} M_0(\bar{\rho}')\hat{n}_0 \cdot \nabla' G_0(\bar{\rho}, \bar{\rho}')dl' \quad (7)$$

Finally, the RCS from perturbed ocean surface is calculated using the scattered filed from independent segments using the Monte-Carlo method (Franceschetti et al., 2000).

$$\sigma^0{}_{pp} = \lim_{\rho \to \infty} \frac{2\pi\rho}{D}\left\{\left\langle \left|E^s{}_{pp}\right|^2 \right\rangle - \left|\left\langle E^s{}_{pp} \right\rangle\right|^2\right\} \quad (8)$$

where pp = VV or HH, and D is the length of each segment. For a vertically polarized incident wave, the RCS can be easily calculated by the duality theorem.

2) Small Perturbation Method

The SPM has been developed to calculate the microwave scattering from a slightly rough surface (Ulaby et al., 1982). In case of scattering from sea surface, the basis of radar backscattering from ocean surface by the SPM is the Bragg scattering theory, and substantial evidences exists for the validity of Bragg scattering from ocean waves (Plant and Keller, 1990). In this study, we used the SPM to calculate the RCS from perturbed ocean wave for comparison with the MoM and SAR data.

V. RESULTS AND DISCUSSION

The numerical simulation for perturbed sea surface was performed using the MoM and Monte-Carlo method as noted previously. Note that the numerical model computed the modulated RCSs along the orthogonal direction of the ridge axis with 250 m resolution. Simulated RCS variations at C- and X-band are shown in Fig. 7 together with SPM results and SAR intensity.

The RCS obtained by the MoM is comparable with the SAR data in all cases, but the SPM underestimates the RCS modulation in SAR data at both bands. Note the different scales of y-axis for the MoM and SPM results. In case of Fig. 7(a) at C-band, the difference of the relative RCS between SAR and MoM is only about 6%, but the position of the peak value is shifted by approximately 2.3 km from the SAR intensity peak. In Fig. 7(b) of the strip D* in the ENVISAT-ASAR, peak RCS positions of both the MoM and SPM results are located at very similar positions to the position of the C-band SAR image within few hundred meters, but the relative RCS value differs by 20% from the SAR data. The simulated RCS by the MoM at X-band (Fig. 7(c)) shows a similar modulation and peak RCS positions with those of the SAR data. Especially, it reproduces the double peak in the relative RCS of values within 6%, and the peak positions within few hundred meters. The average discrepancies are approximately 11% in the relative RCS and 750 m (3 times of the resolution of scattering model) in the peak position. The tidal current speeds of EFDC at T3 point (Fig. 1(b)) which located the near valleys show the strong currents than KHOA data (Fig. 4(a)). This may cause the overestimate of relative RCS from MoM.

In this study, only the orthogonal current component is assumed to contribute the changes in the waveheight spectrum. However, the parallel current component may also affect the hydrodynamic modulation. Kim et al. (2009) showed good agreement between the bathymetric features and the front lines of SAR intensity modulation by taking into account both the orthogonal and parallel current component. Romeiser and Alpers (1997) and Vogelzang (2001) suggested the importance of the source term in deriving Eq. (4), which describes all relevant physical processes of the hydrodynamic modulation. Especially, Vogelzang (2001) showed the difference of simulated RCS in terms of radar frequency and source term. In this study, we used the linear source term only. Thus, the effect of parallel current component as well as sensitivity analysis for the linear, quadratic

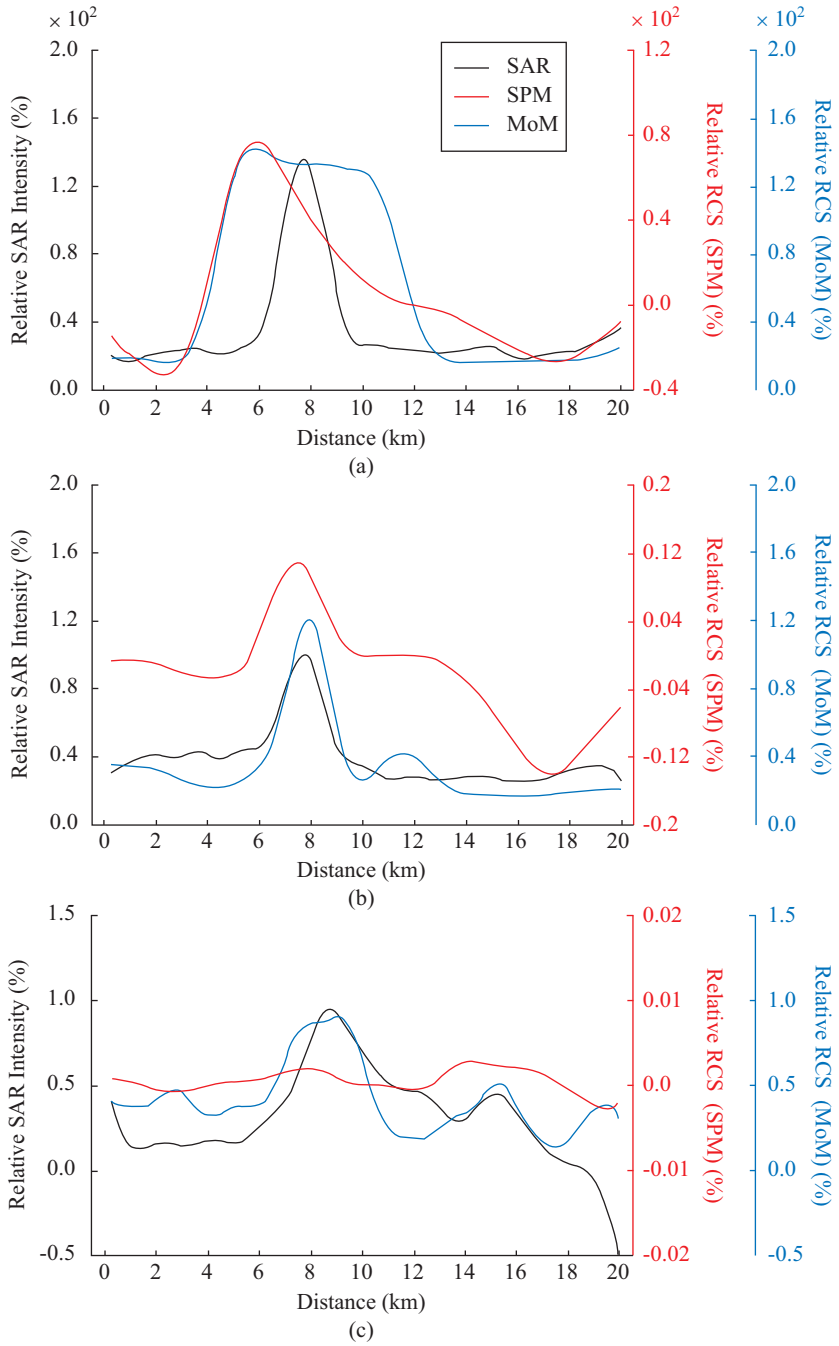

Fig. 7. Comparison of relative SAR image intensity (black), RCS from SPM (red) and MoM (blue). (a) and (b) show the results at strips A* and D* in the ENVISAT-ASAR (C-band) data respectively, and (c) at E* in the TerraSAR-X (X-band) data.

and cubic source term in the wave-current interaction theory are required for the detailed analyses in the future study. As a final remark, it is also desirable to make comparison of our results with ground-truth RCS data such as those acquired by scatterometers on observation towers but there is no such system in Gyeonggi Bay.

VI. CONCLUSION

In this paper, preliminary results are presented on the RCS computed by the numerical radar backscattering model based on MoM and SPM for perturbed sea surface by varying surface current induced by BT at C- and X-bands, and the results are compared with SAR data. It should be noted again that the use of the MoM and Monte-Carlo method was the first of its kind for the study of SAR images of BT. While the SPM model underestimates the RCS than SAR data at X- and C-bands by a substantial amount, the average error of the relative RCS peak value between MoM and SAR data was about 11%, and the

error of peak position was about 750 m. Although there are some discrepancies, reasonable agreement was obtained between the simulated and real SAR image modulation. Further study is being carried out for resolving the observed discrepancy.

ACKNOWLEDGEMENTS

This research was a part of the projects entitled "Development of Ship-handling and Passenger Evacuation Support System", "Construction of Ocean Research Stations and their application Studies, Phase 2", and "Development of Safe Voyage Planning System for Vessels Operating in Northern Sea Route" funded by the Ministry of Oceans and Fisheries, Korea.

REFERENCES

Alpers, W. and I. Hennings (1984). A theory of the imaging mechanism of underwater bottom topography by real and synthetic aperture radar. Journal of Geophysical Research 89, 10529-10546.

Alpers, W. (1985). Theory of radar imaging of internal waves. Nature 314, 245-247.

Broschat, S. L. (1999). Reflection loss from a "Pierson-Moskowitz" sea surface using the nonlocal small slope approximation. IEEE Transactions on Geoscience and Remote Sensing 37(1), 632-634.

Calkoen, C., G. Hesselmans, G. Wensink and J. Vogelzang (2001). The bathymetry assessment system: Efficient depth mapping in shallow seas using radar images. International Journal of Remote Sensing 22, 2973-2998.

Fan, K., W. Huang, H. Lin, J. Pan, B. Fin and Y. Gu (2011). Shallow water depth retrieval from space-borne SAR imagery. Journal of Oceanography 67, 405-413.

Franceshetti, G., A. Iodice and D. Riccio (2000). Scattering from dielectric random fractal surfaces via method of moments. IEEE Transactions on Geoscience and Remote Sensing 38(4), 1644-1655.

Hennings, I. (1998). An historical overview of radar imagery of sea bottom topography. International Journal of Remote Sensing 19(7), 1447-1454.

Hughes, B. A. (1978). The effect of internal waves on surface wind waves: Part 2, theoretical analysis. Journal of Geophysical Research 83(C1), 455-465.

Holliday, D., ST-CYR, G. and N. E. Wood (1986). A radar ocean imaging model for small to moderate incidence angles. International Journal of Remote Sensing 7, 1809-1834.

Hong, D. B., C. S. Yang and K. Ouchi (2015). Estimation of internal wave velocity in the shallow South China Sea using single and multiple satellite images. Remote Sensing Letters 6(6), 448-457.

Jackson, C. R. and J. R. Apel (2004). An Atlas of Internal Solitary-Like Waves and Their Properties. 2nd Edition. Global Ocean Associates, Rockville, MD, USA.

Jackson, C. R., J. C. B. da Silva, G. Jeans, W. Alpers and M. J. Caruso (2013). Nonlinear internal waves in synthetic aperture radar imagery. Oceanography 26(2), 68-79.

Kim, T. (2006). Depth contours appeared on SAR images by interactions between tidal currents and bottom topography. Korean Journal of Remote Sensing 22(5), 415-419.

Kim, T., J. J. Park and B. J. Choi (2009). Study of the tidal channels appeared on SAR image. Korean Journal of Remote Sensing 25(6), 501-505.

Kim, T. H., C. S. Yang, J. H. Oh and K. Ouchi (2014). Analysis of the contribution of wind drift factor to oil slick movement under strong tidal condition: *Hebei Spirit* oil spill case. PLOS ONE 9(1), 1-14.

Kim, T. H., D. B. Hong, C. S. Yang and K. Ouchi (2014). Analysis of the radar backscatter from the sea surface perturbed by varying surface current induced by bottom topography in shallow waters: Comparison of numerical simulation with SAR data. Proceeding of ICSANE, Malacca, 173-177

Kerboal, V. and F. Collard (2005). SAR-derived coastal and marine applications: From research to operational products. IEEE Journal of Oceanic Engineering 30, 472-486.

Lee, G. S., D. C. Kim, Y. K. Seo, H. I. Yi and S. Yoo (2009). Sedimentary Environment and Sequence Study using High Resolution Seismic Survey in Gyunggi Bay, the Yellow Sea. Korean Journal of Fisheries and Aquatic Sciences 42(6), 683-694.

Li, X., C. Li, Q. Xu and W. G. Pichel (2009). Sea surface manifestation of along-tidal-channel underwater ridges imaged by SAR. IEEE Transactions on Geoscience and Remote Sensing 47(8), 2467-2477.

Min, B. I., K. O. Kim, J. H. Yuk, B. H. Choi and K. T. Jung (2011). A harmonic-constants dataset derived from the FDM and FEM tidal models, and real-time tidal prediction for the Yellow and East China Seas. Journal of Coastal Research SI64, 1130-1134.

Ouchi, K. (1994). Modulation of waveheight spectrum and radar cross section by varying curface currents. IEEE Transactions on Geoscience and Remote Sensing 32(5), 995-1003.

Ouchi, K. (2013). Recent trend and advance of synthetic aperture radar with selected topics. Remote Sensing 5(2), 716-807.

Plant, W. J. and W. C. Keller (1990). Evidence of Bragg scattering in microwave Doppler spectra of sea return. Journal of Geophysical Research 95(C9), 16299-16310.

Romeiser, R., W. Alpers and V. Wismann (1997a). An improved composite surface model for the radar backscattering cross section of the ocean surface, 1. Theory of the model and optimization/validation by scatterometer data. Journal of Geophysical Research 102(C11), 25237-25250.

Romeiser, R. and W. Alpers (1997b). An improved composite surface model for the radar backscattering cross section of the ocean surface, 2. Model response to surface roughness variations and the radar imaging of underwater bottom topography. Journal of Geophysical Research 102(C11), 25237-25250.

Seo, S.N. (2008). Digital 30sec gridded bathymetric data of korea marginal seas – KorBathy30s. Journal of Ocean Engineering and Technology 20(1), 110-120.

Shuchman, R. A., D. R. Lyzenga and G. A. Meadows (1985). Synthetic aperture radar imaging of ocean-bottom topography via tidal-current interactions: theory and observations. International Journal of Remote Sensing 6(7), 1179-1200.

Sugimoto, M., K. Ouchi and Y. Nakamura (2013). Comprehensive contrast comparison of laver cultivation area extraction using parameters derived from polarimetric synthetic aperture radar. Journal of Applied Remote Sensing 7, 073566-1-10.

Tsang, L., J. A. Kong, K. H. Ding and C. O. Ao (2001). Scattering of Electromagnetic Waves: Numerical Simulations. A Wiley-Interscience Publication.

Ulaby, F. T., R. K. Moore and A. K. Fung (1982). Microwave remote sensing active and passive. Vol. 2: Radar remote snesing and surface scattering and emission theory. Addison-Wesly Publishing Companay, London.

Valenzuela, G. R. (1978). Theories for the interaction of electromagnetic and oceanic waves-A review. Boundary-Layer Meteorology 13, 61-85.

Valle-Levinson, A., C. Li, K. C. Wong and K. M. M. Lwiza (2000). Convergence of lateral flow along a coastal plain estuary. Journal of Geophysical Research 105(C7), 17045-17061.

Vogelzang, J. (2001). A model comparison study to the imaging of submarine reefs with synthetic aperture radar. International Journal of Remote Sensing 22(13), 2509-2536.

Won, E. S., K. Ouchi and C. S. Yang (2013). Extraction of underwater laver cultivation nets by SAR polarimetric entropy. IEEE Geoscience and Remote Sensing Letters 10(2), 231-235.

Yang, C. S., D. Kim and J. H. Oh (2009). Study on improvement of oil spill prediction using satellite data and oil-spill model: *Hebei Spirit* Oil Spill. Korean Journal of Remote Sensing 25(5), 435-444.